nature geoscience

SUPPLEMENTARY INFORMATION

DOI: 10.1038/NGEO1238

Microfossils of sulphur-metabolizing cells in 3.4-billion-year-old rocks of Western Australia

David Wacey, Matt R Kilburn, Martin Saunders, John Cliff and Martin D Brasier

Supplementary Figures

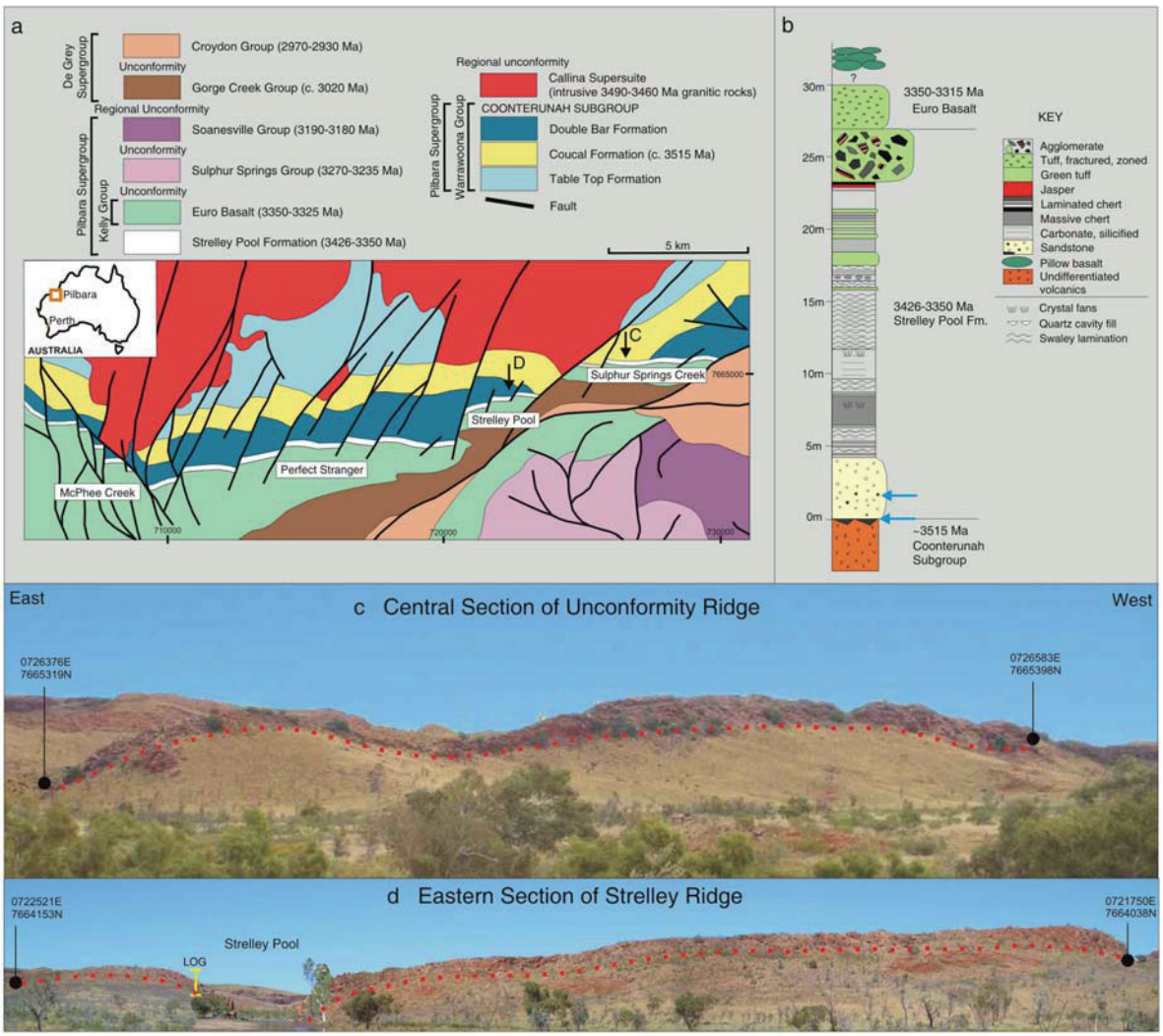

Supplementary Figure 1. a, Geologic setting of the Strelley Pool Formation, East Strelley greenstone belt, Pilbara Craton, Western Australia. Locations of photographs in (c) and (d) are indicated (*modified from ref. 31*). **b**, Generalised stratigraphic log through the Strelley Pool Formation in the East Strelley greenstone belt. Microfossils occur in black sandstone at the base of the formation, often infilling small channels in the ancient land surface, and in reworked clasts up to 2 m higher in the sandstone member (blue arrows). **c** and **d**, Field photographs of the Strelley Pool Formation in the vicinity of the type locality at Strelley Pool, looking south. The ~3400 Ma formation outcrops as steeply southward-dipping ridges, sitting unconformably above eroded volcanic rocks of the ~3515 Ma Coonterunah Subgroup, and overlain by silicified ash and pillow basalt of the 3350-3325 Ma Euro Basalt (not seen here). The basal unconformity lies along the surface indicated by the red dotted line. Microfossils are most abundant in samples from these two ridge sections, just above this basal unconformity surface. Samples used in this study beginning SPU and SPV come from Unconformity Ridge, those beginning SPZ, SPD and SP9 come from Strelley Ridge. Samples beginning SPT come from Wilson Ridge immediately east of Unconformity Ridge, and samples beginning SPE come from Six Mile Ridge immediately west of Strelley Ridge.

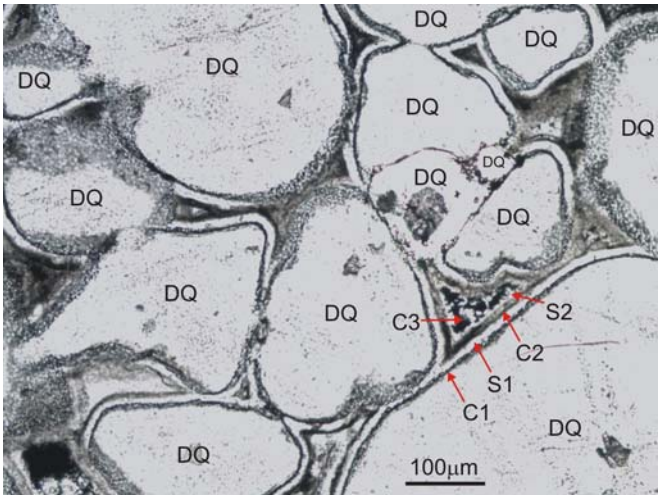

Supplementary Figure 2. Thin section photomicrograph showing multiple generations of carbonaceous material and isopachous silica cements within the Strelley Pool sandstone (sample SPU1). In this sample, detrital quartz grains (DQ) were coated by a thin layer (10-20 µm) of carbon (C1), interpreted as a biolfilm. The biofilms appear thicker on some grains (e.g., top right of image), however, this is mostly an optical illusion caused by the curvature of the grain boundaries within the 30 µm thick thin section. Micron-sized pyrite grains are common within these biofilms. Subsequently, up to c. 30 µm of silica precipitated, partially filling the void space between the detrital quartz grains. A second biofilm (C2) then colonized the surface of the S1 silica. This is often thicker than C1 and in places completely fills the remaining pore space. In the larger pore spaces, a second generation of silica cement precipitated (S2), together with a third generation of carbon (C3). Cells and sheaths are common in the C1 and C2 fabrics, and are only rarely associated with C3. Field and petrographic observations dictate that each of these carbon and silica generations occurred prior to deposition of the overlying chert and Euro Basalt.

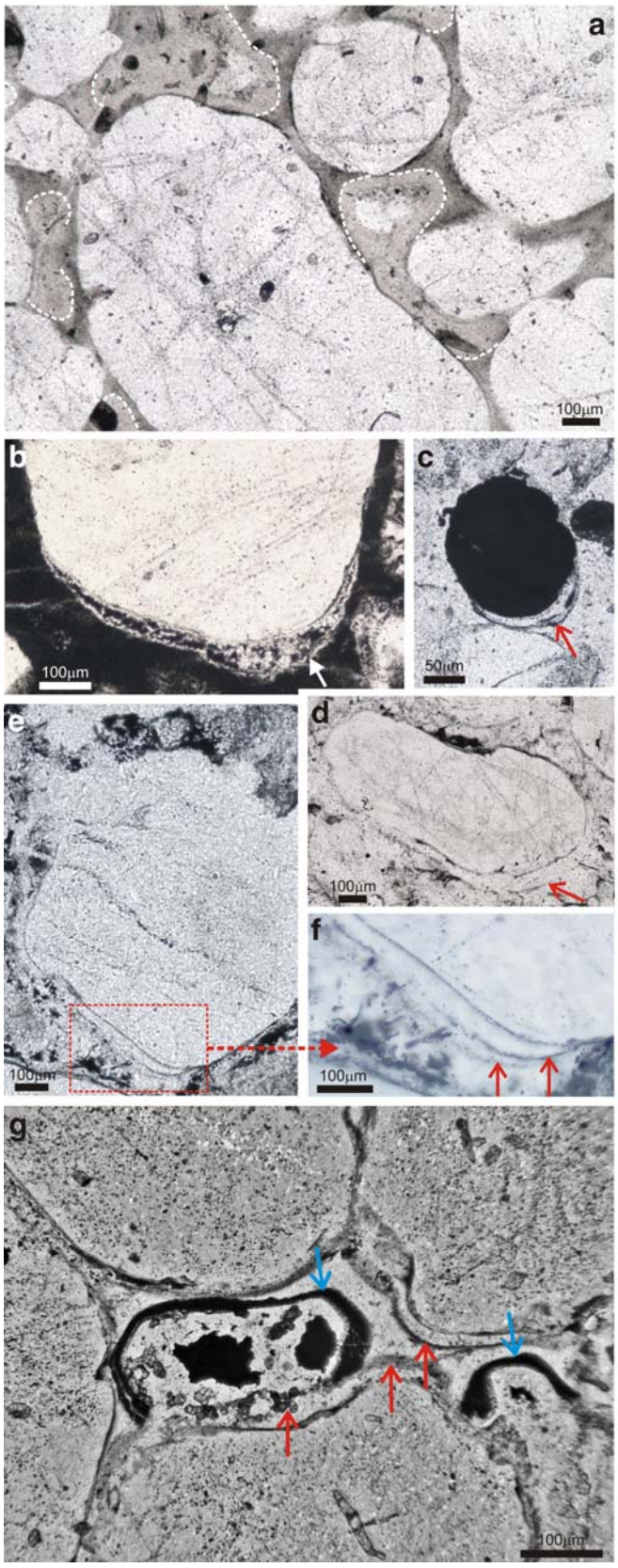
a
100μm
b
100μm
c
50μm
d
100μm
e
100μm
f
100μm
g
100μm

Supplementary Figure 3. Examples of meniscus and dripstone cements seen in petrographic thin sections from the basal Strelley Pool sandstone (samples SPT5, SPV2, SPV3a, c, SPZ2a). These can be taken to imply the development of air-filled pore spaces. **a**, Rounded grains of detrital quartz with chert-filled pore spaces, here divided (by white dotted line) into an outer, early generation of darker, carbon-rich chert with meniscus-like pinching and swelling; and a later infilling of paler chert. **b**, Rounded quartz grain separated from a carbon-rich chert infilling by a dripstone cement (white arrow) provided with a biofilm-like coating. **c**, Rounded grain of detrital pyrite (black grain) from which hangs a dripstone chert cement provided with a carbon coating (red arrow). **d-f**, Rounded grains of detrital quartz having thin carbonaceous envelopes of variable thickness (black) from which hangs a dripstone chert cement (red arrow). (f) shows detail of (e), revealing two successive layers of chert and three biofilm-like carbon-coatings. **g**, Rounded grains of detrital quartz (grey) enclosing pore spaces coated with isopachous cements and carbonaceous cells (red arrows), later infilled with a meniscus cement of carbon-coated chert (blue arrows).

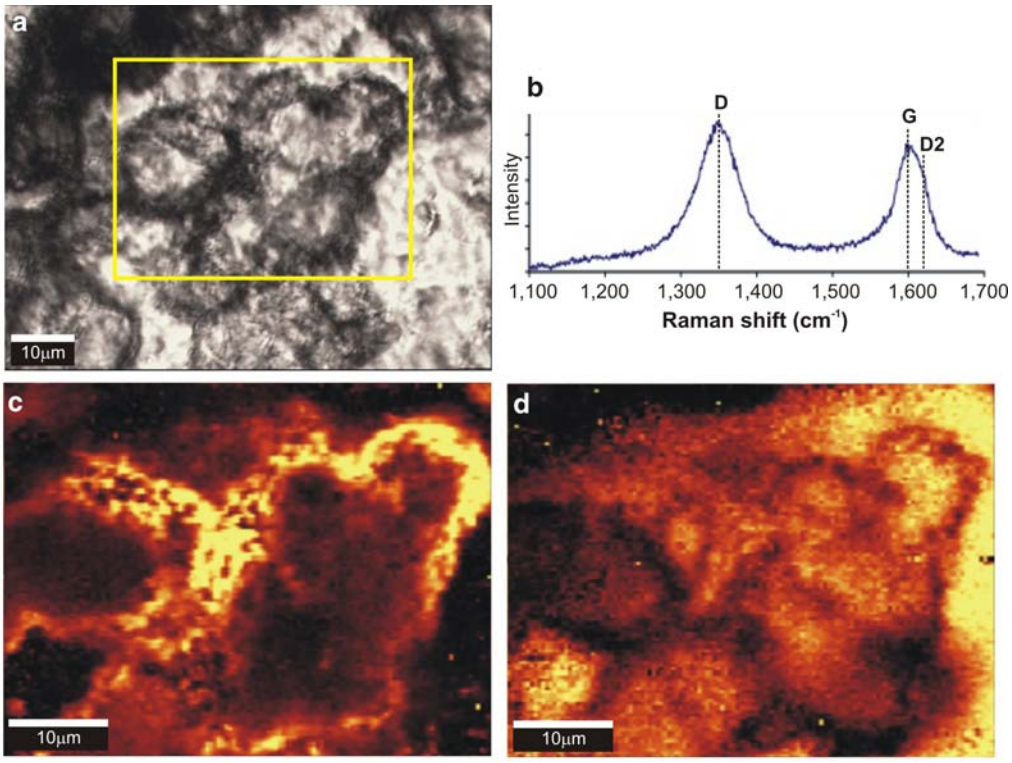

Supplementary Figure 4. In situ Laser Raman micro-spectroscopy of cells within the Strelley Pool sandstone (sample SPV3c). **a**, Transmitted light photomicrograph showing area (boxed) analysed in (b-d). **b**, Part of the first order Raman spectrum from the carbon comprising the cell walls. Two carbon peaks are observed; the ordered 'G' peak at ~1600cm^{-1}, and the disordered 'D' peak at ~1350cm^{-1}. A shoulder to the G peak (D2) is also observed at ~1620cm^{-1}. The position and ratios (area and height) of these peaks is consistent with the known metamorphic grade (lower greenschist facies) of the Strelley Pool sandstone. **c**, Map of the intensity distribution of the carbon G peak showing correlation between carbon and the cell walls. **d**, Map of the intensity distribution of the quartz 465cm^{-1} peak showing the mineralizing quartz phase.

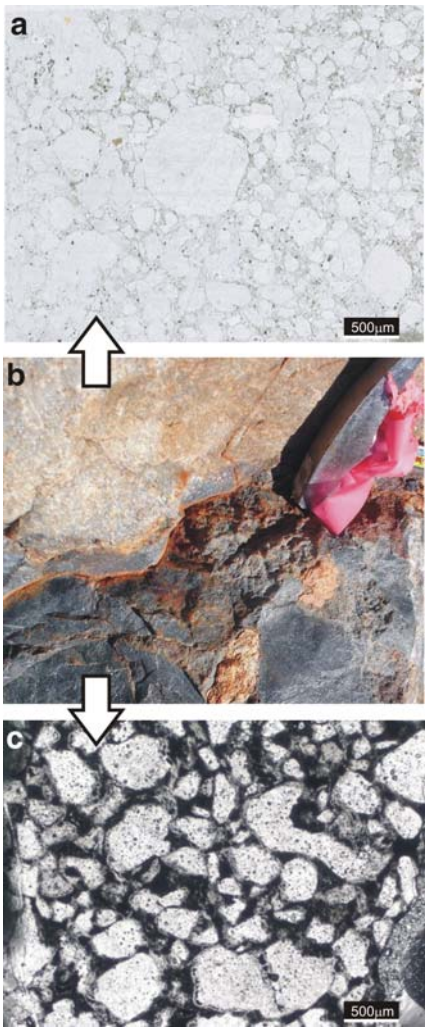

Supplementary Figure 5. Contrasts between pale carbon- and pyrite-poor sandstone and black carbon- and pyrite-rich sandstone from the base of the Strelley Pool Formation (Six Mile Ridge). **a**, Thin section photomicrograph of carbon/pyrite-poor sandstone from area indicated in outcrop image below. **b**, Outcrop photograph showing difference between black carbon/pyrite-rich sandstone and pale carbon/pyrite-poor sandstone. Geological hammer-head is c.15 cm across. **c**, Thin section photomicrograph of carbon/pyrite-rich sandstone from area indicated in (b) above.

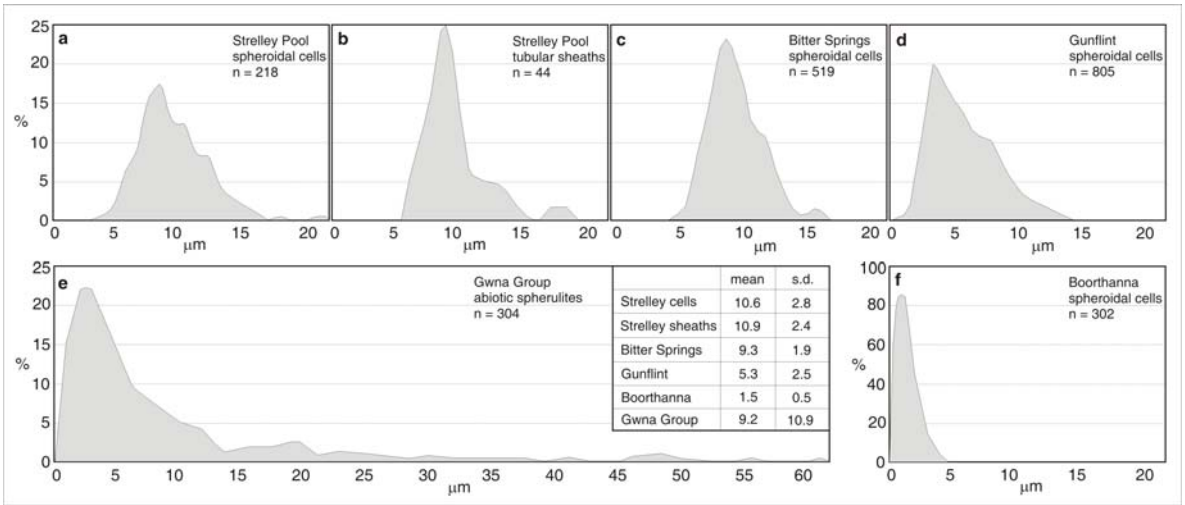

Supplementary Figure 6. Frequency distributions (FD) of microfossils from the c. 3400 Ma Strelley Pool sandstone compared to those from three younger biological microfossil assemblages and one abiotic spherulite assemblage. **a**, FD of spheroidal cells from thin section SPV3a of the Strelley Pool sandstone. Note that this particular thin section does not contain any of the rare examples of large (>25 μm) spheroidal microfossils (e.g., Fig. 1g). **b**, FD of tubular sheaths from thin section SPV3a of the Strelley Pool sandstone. **c**, FD of spheroidal cells from the c. 800 Ma Bitter Springs Formation, Central Australia (*data from ref. 32*). **d**, FD of spheroidal cells from the c. 1900 Ma Gunflint Formation, Ontario (*data from ref. 32*). **e**, FD of abiotic spherulites from a jaspilitic chert of the c. 560 Ma Gwna Group, Wales (*data from ref. 33*). **f**, FD of small spheroidal cells from the c. 800 Ma Boorthanna Formation, South Australia (*data from ref. 33*). Note that the five biological assemblages show a positively skewed FD and small relative standard deviations (s.d.). In contrast, the abiotic spherulites show a power law FD with a long positive tail, and a large standard deviation. Mean and s.d. measurements are in microns.

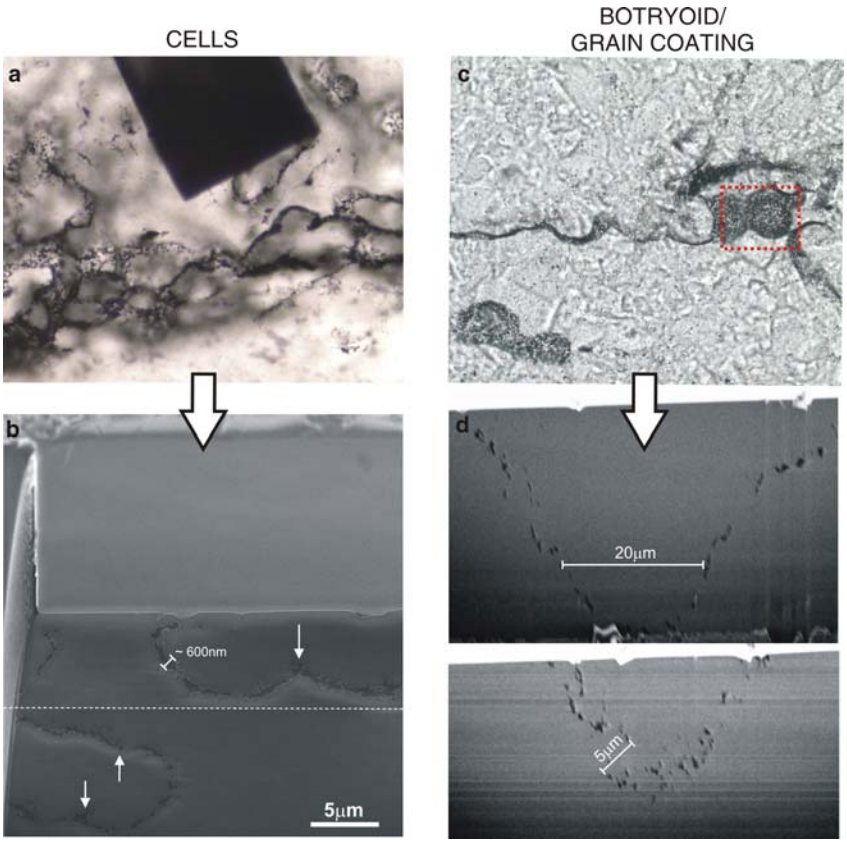

Supplementary Figure 7. Subsurface microstructure of Strelley Pool sandstone microfossils contrasted with that of grain coatings/botryoids within thin sections of the same unit (sample SPV3c). **a**, Thin section photomicrograph after focused ion beam (FIB) milling and **b** SEM image of FIB-milled face showing cross-sections through two microfossils interpreted as chains of cells. Note consistency of width of the cell walls and partial septa separating adjacent cellular compartments (arrows). Black trench in (a) indicates approximate volume milled by the FIB. **c**, Thin section photomicrograph prior to FIB-milling (box represents FIB-milled area) and **d** SEM images of two FIB-milled faces showing cross sections through a carbon-coated botryoidal structure. Note relatively large size, lack of coherent wall fabric, and variable width of botryoid pseudowalls.

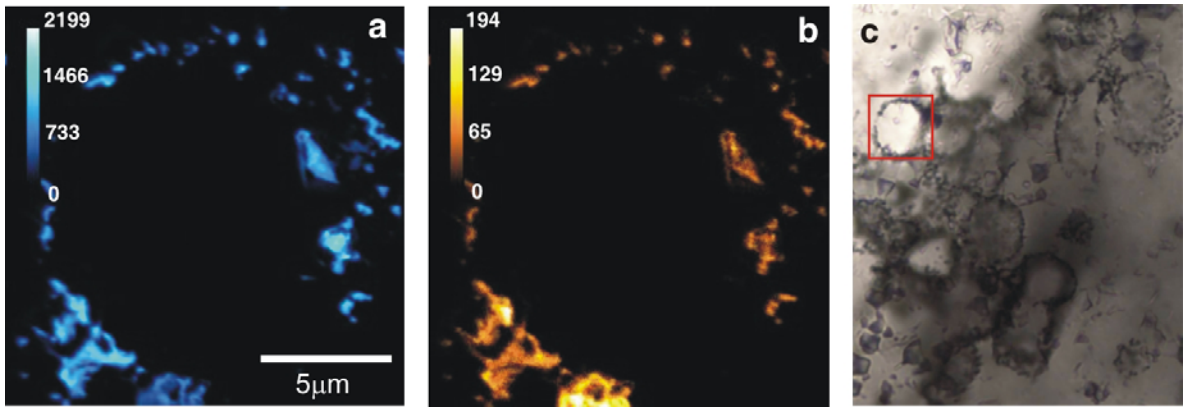

Supplementary Figure 8. Microfossil chemistry (sample SPV3b). **a**, NanoSIMS carbon ($^{12}C^-$) ion map. **b**, NanoSIMS nitrogen ($^{12}C^{14}N^-$) ion map. **c**, Thin section photomicrograph showing in situ area of NanoSIMS analysis (boxed).

Supplementary Methods

IMS 1280 carbon isotope methodology

Carbon isotopes (^{12}C and ^{13}C) were analysed using the CAMECA IMS1280 of the Centre for Microscopy Characterisation and Analysis (CMCA) at The University of Western Australia. Analyses were conducted on 100 µm thick standard polished thin-sections cut into c. 5 x 5 mm squares that were mounted with a chip of a graphite disc CMCA-G1 standard ($\delta^{13}C$ = -25.84‰ ± 0.04, VPDB) embedded in resin. The two samples (SPZ2b – carbonaceous/pyritic sandstone containing abundant microfossils; SP9-D2a – carbonaceous/pyritic sandstone with rare microfossils) were first mapped in reflected light

and these images were used to locate regions of interest when the sample was placed in the IMS 1280. The sample was coated with a 30 nm gold coat to provide conductivity at high voltage. Data were obtained in a single c. twelve-hour analytical session.

The instrument was operated in multicollection mode using dual faraday cup detectors at a nominal mass resolution of 2500, using a focused, +10 keV, ~ 2 nA Cs^+ primary beam with an impact energy of 20 keV. Secondary instrument parameters were set as follows: contrast and field apertures, 4000 μm; entrance slit, 120 μm; exit slits, 500 μm; energy slit, 40 eV with a 5 eV band gap; magnification, 130x; The sample area was presputtered for 60 seconds with a 35 μm x 35 μm rastered beam. Automated secondary beam centering and analyses were performed using a 25 μm x 25 μm raster using dynamic transfer. Although the graphitic carbon targets are conductors, the normal incidence electron flood gun was utilised for charge compensation in the event that the primary ion beam overlapped onto insulating matrix silica minerals. Magnetic field stability was maintained using NMR regulation.

Correction for instrumental mass fractionation (IMF) was adapted from the method of Kita *et al*[34], α was determined as the weighted mean of individual drift and background corrected standard determinations α_i:

$$\alpha_i = \frac{1 + \delta^{13}C_{raw} / 1000}{1 + \delta^{13}C_{PDB} / 1000} \qquad [1]$$

where $\delta^{13}C_{raw}$ is equal to the δ value of the drift and background corrected $^{13}C/^{12}C$ ratio relative to PDB (0.0112372) and $\delta^{13}C_{PDB}$ is the $\delta^{13}C$ of the CMCA-G1 graphite standard (-25.84‰). Single analyses are corrected to the PDB scale using:

$$\delta^{13}C = \left[\left(1 + \delta^{13}C_{raw} / 1000\right) / \alpha - 1\right] * 1000 \quad [2]$$

Uncertainties associated with individual $\delta^{13}C$ estimates were calculated using standard propagation of error techniques[35]. External precision on 46 bracketing $\delta^{13}C$ standard analyses was 0.3‰ (1σ). Sample count rates were as low as 2% of the count rate of the standard, however, there was no observed correlation between secondary count rate and $\delta^{13}C$ of the samples ($\rho = 0.07$, $p = 0.6$). Analyses from clusters of microfossils have a similar $\delta^{13}C$ range to nearby patches of black amorphous carbon, inconsistent with later contamination or instrumental artefacts.

NanoSIMS analysis

NanoSIMS ion mapping was performed using the CAMECA NanoSIMS 50 in CMCA at the University of Western Australia. The samples consisted of 30 μm and 100 μm polished thin-sections (Samples SP9-D2b, SPV3b), cut into a c. 12 x 8 mm rectangle, mounted in resin alongside a c. 10 x 10 mm chip of a the CMCA-G1 standard, and placed in a 25 mm diameter CAMECA sample holder. The holder and contents were mapped in reflected light and these images were used to navigate to regions of interest once the sample was in the NanoSIMS. A 5 nm gold coat was applied to provide conductivity at high voltage.

All measurements were obtained with a c. 100 nm Cs^+ primary ion beam, with a net impact energy of c. 16 kV, and a beam current of c. 2.9 pA. The NanoSIMS was operated in multi-collector mode, allowing multiple ion species to be collected simultaneously from the same scanned area. The sample surface was presputtered with the primary ion beam (using 17.4 pA beam current; D1=1) to > 5 x 10^{16} ions/cm^2 (cf. 36) in order to remove surface contamination, implant Cs^+ ions and reach a steady-state of ion emission. Charge compensation was achieved by using the electron flood gun. Secondary ion images were obtained by rastering the primary ion beam across areas measuring between 6 x 6 μm and 18 x 18 μm, at a resolution of 256 x 256 pixels (each pixel measuring between 23 nm and 70 nm), with dwell times of between 5 ms and 30 ms per pixel.

Focussed ion beam (FIB) preparation of TEM and SEM samples

A dual-beam FIB system (FEI Helios NanoLab) at Adelaide Microscopy, University of Adelaide was used to prepare microfossil TEM samples from standard uncovered polished geological thin sections coated with c.5 nm of platinum. Electron beam imaging was used to identify microfossils of interest in the polished thin sections allowing site-specific TEM samples to be prepared. The TEM sections were prepared by a series of steps involving different beam energies and currents[37]. The resulting TEM sections were extracted using an in-situ micromanipulator and attached to Omniprobe® copper TEM grids via platinum connects prior to final thinning to a thickness of ~100 nm. FIB preparation of TEM sections allows cellular features below the surface of the thin sections to be targeted, thus eliminating the risk of surface contamination producing artefacts. Morphological analysis

using FIB-SEM was performed on standard uncovered geological thin sections using dual-beam FIB systems at Adelaide Microscopy (FEI Helios NanoLab) and the Naval Postgraduate School, California (Zeiss Neon 40).

TEM analysis

TEM data were obtained using a JEOL 2100 LaB_6 TEM equipped with a Gatan Orius CCD camera and Tridiem energy filter operating at 200 kV, located in CMCA at The University of Western Australia. Energy-filtered TEM elemental maps were obtained using the conventional three-window technique[38], with energy windows selected to provide optimum signal-to-noise. Selected area electron diffraction (SAED) was performed using an aperture that selected a 200 nm diameter area of the FIB section.

Raman Analysis

Raman was performed at the Carnegie Institute, Washington, using a WITec a-Scanning Near-Field Optical Microscope customized to incorporate confocal Raman spectroscopy imaging. The excitation source was a frequency-doubled solid-state YAG laser (532 nm) operating between 1-20 mW output power, with a range of objective lenses up to 100x and a 50 μm optical fibre acting as the confocal pin hole. Imaging and single spectra operational modes were both used during this study, with the laser focussed to z = c.5 μm below the surface of the thin section to eliminate surface contamination.

	Microfossils from Sugitani et al., 2010	Microfossils from this report
Age (Ma)	3350-3426 Ma Strelley Pool Formation	3350-3426 Ma Strelley Pool Formation
Relative age	Younger – found within chert unit overlying basal sandstone	Older – found within basal sandstone underlying chert unit.
	Based on relative stratigraphic positions there may be as much as 50 Ma between the two assemblages	
Location	Panorama, Warralong and Goldsworthy greenstone belts (Sugitani et al., 2010, fig.1)	East Strelley greenstone belt (Supp. Fig.1)
	The greenstone belts are between 30 and 100km apart	
Host lithology	Primary carbonaceous chert	Silicified sandstone
Morphologies	1. Small spheroids <15µm and large spheroids 15-100µm 2. Lenticular and spindle shapes 3. Threads 4. Films	1. Small spheroids and ellipsoids 5-25µm diameter 2. Rare (<10 examples) large spheroids up to 80µm diameter 3. Tubular shapes 7-20µm diameter
Distribution	In carbonaceous layers within the chert – abundant and locally associated with pyrite; Small spheroids often in colonies and associated with films; Large spheroids and spindles mostly solitary	Within early silica cements coating sand grains, and in silica filled pore spaces; abundant; closely associated with pyrite; Spheroids and ellipsoids often in chains and colonies; Tubes can be closely packed together
Geochemistry	Laser Raman shows carbonaceous composition and expected thermal maturity – some small variations in composition between greenstone belts and even across thin sections; Bulk $\delta^{13}C$ from -31.01 to -36.75‰	Laser Raman and TEM shows carbonaceous composition, expected thermal maturity and similarity to Sugitani et al., 2010; In situ $\delta^{13}C$ from -33 to -46‰; $\delta^{34}S$ from -12 to +6‰ and $\Delta^{33}S$ from -1.65 to +1.43‰ (from co-occurring micro-pyrite); Enrichments of microfossil walls in nitrogen ± sulphur
Taphonomic features	Variable preservation from hyaline to granular to indistinct degraded microfossil walls; Some deformation (folding, wrinkling and breakage) of microfossil walls and films; Partial 3D preservation in early silica	Variable preservation from hyaline to granular to partially degraded microfossil walls; Some deformation (folding and breakage) of microfossil walls; 3D preservation by early silica cementation

Supplementary Table 1. Comparison of microfossils from the Strelley Pool sandstone (this report) with those from the overlying Strelley Pool chert reported by Sugitani et al. (*ref. 17 of main article*).

Supplementary Table 2

Analysis ID	$\delta^{13}C_{PDB}$ (‰)	$\pm 2\sigma_{ext}$	Analysis ID	$\delta^{13}C_{PDB}$ (‰)	$\pm 2\sigma_{ext}$
Session standards			Session unknowns		
GD-1.1	-26.03	0.20	SPZ-1.1	-44.42	3.73
GD-1.2	-25.74	0.20	SPZ-1.2	-37.70	1.86
GD-1.3	-25.94	0.17	SPZ-1.3	-39.79	2.04
GD-1.4	-25.99	0.18	SPZ-1.4	-45.97	2.98
GD-1.5	-26.74	0.21	SPZ-1.5	-45.54	2.04
GD-1.6	-25.18	0.18	SPZ-1.6	-33.79	3.49
GD-1.7	-25.71	0.19	SPZ-1.7	-41.45	1.68
GD-1.8	-25.97	0.17	SPZ-1.8	-38.53	2.72
GD-1.9	-26.96	0.15	SPZ-1.9	-40.23	2.94
GD-1.10	-25.52	0.16	SPZ-1.10	-40.40	1.87
GD-1.11	-25.42	0.16	SPZ-1.11	-40.10	3.13
GD-1.12	-25.92	0.20	SPZ-1.12	-42.70	3.63
GD-1.13	-25.15	0.17	SPZ-1.13	-37.37	1.46
GD-1.14	-26.04	0.15	SPZ-1.14	-43.04	2.42
GD-1.15	-25.87	0.16	SPZ-1.15	-43.05	2.77
GD-1.16	-25.94	0.17	SPZ-1.16	-39.22	0.70
GD-1.17	-26.08	0.15	SPZ-1.17	-42.47	2.86
GD-1.18	-25.58	0.16	SPZ-1.18	-40.52	1.34
GD-1.19	-26.29	0.22	SPZ-1.19	-39.04	1.89
GD-1.20	-25.72	0.17	SPZ-1.20	-37.75	1.02
GD-1.21	-26.13	0.20	SPZ-1.21	-39.85	2.79
GD-1.22	-25.99	0.22	SPZ-1.22	-38.65	2.36
GD-1.23	-26.26	0.19	SPZ-1.23	-38.42	3.21
GD-1.24	-25.91	0.20	SPZ-1.24	-36.43	2.98
GD-1.25	-25.57	0.23	SPZ-1.25	-42.12	3.53
GD-1.26	-25.81	0.24	SPZ-1.26	-39.43	1.00
GD-1.27	-25.70	0.25	SPZ-1.27	-39.74	1.49
GD-1.28	-26.01	0.40	SPZ-1.28	-41.40	2.90
GD-1.29	-25.90	0.39	SPZ-1.29	-40.60	2.07
GD-1.30	-25.62	0.39	SPZ-1.30	-41.07	3.74
GD-1.31	-25.89	0.26	SPZ-1.31	-41.87	2.16
GD-1.32	-26.04	0.26	SPZ-1.32	-42.57	2.08
GD-1.33	-25.86	0.24	SPZ-1.33	-37.24	1.29
GD-1.34	-26.13	0.18	SPZ-1.34	-40.29	1.66
GD-1.35	-25.50	0.18	SPZ-1.35	-43.28	3.57
GD-1.36	-25.46	0.20	SPZ-1.36	-41.10	3.27
GD-1.37	-26.32	0.23	SPZ-1.37	-39.64	3.34
GD-1.38	-25.47	0.21	SPZ-1.38	-41.03	1.11
GD-1.39	-25.71	0.20	SPZ-1.39	-40.00	1.04
GD-1.40	-25.85	0.25	SPZ-1.40	-38.67	1.17
GD-1.41	-26.20	0.26	SPZ-1.41	-38.35	2.05
GD-1.42	-25.59	0.28	SPZ-1.42	-38.49	0.99
GD-1.43	-25.78	0.40	SPZ-1.43	-38.95	2.17
GD-1.44	-25.97	0.43	SPZ-1.44	-39.81	3.09
GD-1.45	-25.81	0.44			
			SP9-1.1	-36.94	3.19
			SP9-1.2	-43.21	3.00
			SP9-1.3	-32.85	3.69
			SP9-1.4	-38.23	3.77
			SP9-1.5	-38.19	3.71
			SP9-1.6	-41.62	3.55
			SP9-1.7	-38.96	2.18
			SP9-1.8	-41.39	1.85
			SP9-1.9	-33.49	3.24
			SP9-1.10	-35.83	2.25

Supplementary Table 2. In situ carbon isotope data from the Strelley Pool sandstone. Errors on the sample data are of a similar magnitude to those of previous ion microprobe $\delta^{13}C$ data from carbonaceous microstructures[39-41]. Our range of data is remarkably similar to that from bona fide microfossils from the 1900 Ma Gunflint Formation (-32.4‰ to -45.4‰)[39]. Our $\delta^{13}C$ data is consistent with biological fractionations taking place during autotrophic carbon fixation via either the reductive acetyl-CoA pathway or the Calvin cycle[41]. It is notable that our $\delta^{13}C$ data are mostly too negative to be attributed to isotopic fractionation by cyanobacteria, and mostly too positive to be attributed to isotopic fractionation by methanogens[cf.42]. However, they do mostly lie within the $\delta^{13}C$ range reported for SRB biomass in modern settings[43] (*also see fig. 9 of ref. 40*).

Supplementary References

31. Wacey, D. Stromatolites in the ~3400Ma Strelley Pool Formation: examining biogenicity from the macro- to the nano-scale. *Astrobiol.* **10**, 381-395 (2010).

32. Schopf, J. W. Are the oldest 'fossils', fossils? *Origins of Life* **7**, 19-36 (1976).

33. Brasier, M. D., McLoughlin, N., Green, O. & Wacey, D. A fresh look at the fossil evidence for early Archaean cellular life. *Phil. Trans. R. Soc. B* **361**, 887-902 (2006).

34. Kita, N. T., Ushikubo, T., Fu, B. & Valley, J. W. High precision SIMS oxygen isotope analysis and the effect of sample topography. *Chem. Geol.* **264**, 43-57 (2009).

35. National Institute of Standards and Technology, *NIST Technical Note* **1297** (1994).

36. Gnaser, H. Ionization probability of sputtered cluster anions: C_n^- and Si_n^-. *Appl. Surf. Sci.* **203-204**, 78–81 (2003).

37. Giannuzzi, L. A. & Stevie, F. A. *Introduction to Focused Ion Beams: Instrumentation, Theory, Techniques, and Practise*, Springer-Verlag, New York (2005).

38. Brydson, R. *Electron Energy Loss Spectroscopy*, Springer-Verlag, New York (2001).

39. House, C. H. *et al.* Carbon isotopic composition of individual Precambrian microfossils. *Geology* **28**, 707-710 (2000).

40. Ueno, Y., Isozaki, Y., Yurimoto, H. & Maruyama, S. Carbon isotopic signatures of individual Archean microfossils(?) from Western Australia. *Int. geol. Rev*. **43**, 196-212 (2001).

41. Schidlowski, M., Hayes, J. M. & Kaplan, I. R. Isotopic inferences of ancient biochemistries: carbon, sulfur, hydrogen, and nitrogen. In Schopf, J. W. (Ed.) *Earth's Earliest Biosphere*, Princeton University Press, 149-186 (1983).

42. Ueno, Y., Yamada, K., Yoshida, N., Maruyama, S. & Isozaki, Y. Evidence from fluid inclusions for microbial methanogenesis in the early Archaean era. *Nature* **440**, 516-519 (2006).

43. Londry, K. L. & Des Marais, D. J. Stable carbon isotope fractionation by sulfate-reducing bacteria. *App. Environ. Microbiol.* **69**, 2942-2949 (2003).